Published in final edited form as:

Cell. 2021 September 02; 184(18): 4669–4679.e13. doi:10.1016/j.cell.2021.07.034.

Molecular mechanism of prestin electromotive signal amplification

Jingpeng Ge[1,4], **Johannes Elferich**[1,4], **Sepehr Dehghani-Ghahnaviyeh**[2], **Zhiyu Zhao**[2], **Marc Meadows**[1], **Henrique von Gersdorff**[1], **Emad Tajkhorshid**[2], **Eric Gouaux**[1,3,5,*]

[1]Vollum Institute, Oregon Health & Science University, 3181 SW Sam Jackson Park Road, Portland, OR 97239

[2]Department of Biochemistry, NIH Center for Macromolecular Modeling and Bioinformatics, Center for Biophysics and Quantitative Biology, and Beckman Institute for Advanced Science and Technology, University of Illinois at Urbana-Champaign, Urbana, IL 61801

[3]Howard Hughes Medical Institute, Portland, OR 97239

[4]These authors contributed equally to this work

[5]Lead contact

Summary

Hearing involves two fundamental processes: mechano-electrical transduction and signal amplification. Despite decades of studies, the molecular basis for both remain elusive. Here we show how prestin, the electromotive molecule of outer hair cells (OHCs) that senses both voltage and membrane tension, mediates signal amplification by coupling conformational changes to alterations in membrane surface area. Cryo-EM structures of human prestin bound with chloride or salicylate, at a common ‘anion site’, adopt contracted or expanded states, respectively. Prestin is ensconced within a perimeter of well-ordered lipids, through which it induces dramatic curvature of the membrane and couples protein conformational changes to the bulk membrane. Together with computational studies, we illustrate how the anion site is allosterically coupled to changes in the transmembrane domain cross-sectional area and the surrounding membrane. These studies provide critical insight into OHC electromotility by providing a structure-based mechanism of the membrane motor prestin.

Keywords

Hearing; cochlear amplification; cryo-EM; protein lipid interaction; prestin; electromotility

*Correspondence: gouauxe@ohsu.edu.

Author contributions

J.G and E.G designed the project. J.G performed biochemistry, cryo-EM data collection and processing, and model building; J.G and J.E performed the prestin NLC measurement with the dual-sine method; M.M and H.v.G performed the prestin NLC measurement with the “sine+DC” method; S.D, Z.Z and E.T performed MD simulations; J.G and J.E wrote the draft of the manuscript. All authors contributed to editing and manuscript preparation.

Declaration of interests

The authors declare no competing interests.

Introduction

Hearing is the final sensory modality for which there is, at present, no molecular mechanism. The outer hair cells (OHCs) in the mammalian cochlea are crucial to hearing because they mediate signal amplification via an active mechanical feedback that enhances the sensitivity and frequency selectivity of sound stimuli (Ashmore, 2019; Dallos, 2008; Santos-Sacchi et al., 2017). Loss of OHCs due to excessive noise, ototoxic drugs, or normal aging leads to reduction of sound sensitivity and ability to distinguish sounds (Gummer and Preyer, 1997). Driven by changes in membrane potential, OHCs exhibit fast changes in length along the axial direction at acoustic frequencies up to 80 kHz (Ashmore, 1987; Brownell et al., 1985; Forge, 1991), deemed electromotility (eM). eM is defined by classic electrical signatures, including charge movements across the electric field and non-linear capacitance (NLC) (Santos-Sacchi, 1991). Prestin, a member of SLC26 anion transporter family, is the motor protein responsible for the fast eM of OHCs (Zheng et al., 2000) and is abundantly expressed in the OHC lateral membrane (Gale and Ashmore, 1997; Huang and Santos-Sacchi, 1993; Mahendrasingam et al., 2010). Prestin acts directly on the lateral membranes and derives energy from the OHC's transmembrane potential, which together with its fast kinetics set it apart from other molecular motors, such as cytoskeletal or rotary motors (Dallos and Fakler, 2002; Guo et al., 2016). The deletion of prestin in mice results in the loss of eM, shortened OHCs and a reduction of hearing sensitivity of 40–60 dB (Liberman et al., 2002). Mutations in human prestin are associated with deafness (Mutai et al., 2013).

Prestin has been described as an 'incomplete transporter' (Oliver et al., 2001; Zheng et al., 2000) that transits from an expanded state to a contracted state coupled with a positive net charge moving across the membrane (Dallos et al., 2006; Iwasa, 1994; Santos-Sacchi and Song, 2014). Evidence suggests prestin forms dimers (Chi et al., 2020; Walter et al., 2019) or tetramers (Hallworth and Nichols, 2012; Zheng et al., 2006), thus leaving the oligomeric state unresolved. Intracellular anions, particularly chloride, are indispensable for the normal function of prestin and regulate the eM of prestin, including shifting the NLC voltage dependence (Oliver et al., 2001; Rybalchenko and Santos-Sacchi, 2008b), affecting the transition rate of prestin (Santos-Sacchi and Song, 2016; Song and Santos-Sacchi, 2013), and regulating the frequency response of the cochlea (Santos-Sacchi et al., 2006). Salicylate, a widely used drug, reversibly inhibits eM and causes hearing loss or tinnitus at high doses (Kakehata and Santos-Sacchi, 1996; Mongan et al., 1973; MYERS and BERNSTEIN, 1965). The importance of anions to prestin function initially suggested that chloride acts as an extrinsic voltage sensor (Oliver et al., 2001), but more recent evidence suggested that anions, such as chloride, play an allosteric role (Rybalchenko and Santos-Sacchi, 2003; Rybalchenko and Santos-Sacchi, 2008b; Song and Santos-Sacchi, 2010). Prestin is also sensitive to membrane tension (Iwasa, 1993; Santos-Sacchi et al., 2001) and the diffusion of prestin in the membrane is regulated by cholesterol (Kamar et al., 2012; Rajagopalan et al., 2007; Sfondouris et al., 2008). Here, we carry out single-particle cryo-EM microscopy, molecular dynamics simulation and electrophysiology to illuminate multiple high resolution structures of prestin and to provide a structural basis for its

electromotive, membrane-sensitive properties, thereby providing the molecular basis for signal amplification in hearing.

Results and Discussion

Cryo-EM structure of prestin is a domain-swapped dimer

We expressed full-length human prestin fused with a C-terminal green fluorescence protein (GFP) and an affinity tag in HEK293 GnTI^{-} cells (Goehring et al., 2014) for structural and electrophysiological studies. Cells transfected with this construct produced a robust NLC with peak capacitances at −54.0 ± 3.2 mV and −51.4 ± 3.4 mV using dual-sine methodology (Santos-Sacchi et al., 1998) (Figure 1A) and a lock-in “Sine+DC” method (Gillis, 2000) (Figure S1A–S1C), respectively. The NLC was not observed in non-transfected cells (Figure S1A, S1C) and was reversibly inhibited by 10 mM salicylate (Figure 1A), thus demonstrating that this recombinant prestin recapitulates native prestin function.

We screened solubilization conditions for prestin by fluorescence-detection size-exclusion chromatography (FSEC) (Goehring et al., 2014) and found two peaks, suggestive of two distinct oligomerization states, dependent upon detergent solubilization conditions (Figure S2A). Amongst the panel of detergents, glycol-diogenin (GDN) resulted in the greatest fraction of the earlier eluting, hypothetically oligomeric state (Figure S2A). We purified the oligomeric form of prestin, in the presence of chloride, in either GDN micelles (Pres-Cl) or in lipid nanodiscs (Pres-Cl-nanodisc) and employed single particle cryo-EM to elucidate structures at 2.3 Å and 2.7 Å resolution, respectively (Figure 1, Figures S3–S5, Table S1). Reconstructions of prestin from both conditions reveal a dimeric architecture with no other oligomeric state found during data processing, indicating that prestin is a dimer. However, we cannot exclude the possibility that prestin in native OHCs can form higher oligomers due to its high level of expression or interactions with cytosolic scaffolds. We hypothesize that the later eluting SEC peak corresponds to immature, unassembled prestin. The Pres-Cl and Pres-Cl-nanodisc structures are indistinguishable (Cα RMSD: 0.20, Figure S11K, S14A, S14B) and because of the higher resolution and better quality of the Pres-Cl map (Figure S4, S5), we used Pres-Cl for structure illumination unless otherwise mentioned.

Prestin forms a domain-swapped homodimer, with each protomer containing a transmembrane domain (TMD, residues 76–504), an N-terminal domain (NTD, residues 1–75) and a C-terminal sulfate transporter and anti-sigma factor antagonist domain (STAS, residues 505–744) (Figure 1B, 1D). The NTD and STAS domains form a dimerized ‘base’ on the cytoplasmic side of the membrane, on ‘top’ of which two TMDs separately insert into the membrane (Figure 1C, 1D). The TMD adopts the UraA fold (Lu et al., 2011), with a 7+7 inverted helical arrangement that is subgrouped into a ‘core’ domain and a ‘gate’ domain. Though prestin shares a similar fold to the recently resolved SLC26A9 structures (Chi et al., 2020; Walter et al., 2019) with an overall Cα RMSD of 4.6 Å to human SLC26A9 (Figure S7A, S7B), the high resolution cryo-EM structures of prestin reveal significantly different structural features. A chloride ion is located on the interface between the core and gate domains. Over a hundred well-resolved lipid molecules, including two cholesterol molecules in the space between the TMDs (Figure 1C, 1D), reveal the extensive prestin-membrane

interactions and provide the first glimpse of how prestin is inserted into the membrane, induces membrane curvature and couples conformation changes to the bulk membrane.

Both the NTD and STAS domains are crucial for the canonical eM function of prestin (Bai et al., 2006; Navaratnam et al., 2005). The N-terminal residues form an anti-parallel β sheet (Nβ 1) (Figure 1D), and disrupting Nβ 1 abolishes the oligomerization and NLC of prestin (Navaratnam et al., 2005). A partially membrane-embedded region, composed of three short α helices (Nα 2–4) (termed the 'arm' domain), forms a 'paddle' to flank the TMD and is tethered to Nβ1 through a loop spanning the STAS domain. Characteristic features of the prestin STAS domain, compared to that of SLC26A9 (Chi et al., 2020; Walter et al., 2019), include a longer Cα 2 helix of the intervening sequence region (IVS) and a longer Cα 6 helix in the C-terminus (Figure 1D, Figures S6, S7), where mutations of a cluster of the positively charged residues on Cα 2 to negatively charged residues shift the NLC along the voltage axis (Bai et al., 2006) and disruption of Cα 6 abolishes the prestin NLC (Navaratnam et al., 2005). Distinct from the previous crystal structure of the rat prestin STAS domain with a truncated IVS and C terminus (Lolli et al., 2016), the structure of the STAS domain in full-length human prestin is more similar to the structure of the chicken prestin STAS domain (Lolli et al., 2016) and incompatible with the proposed anion binding site in the STAS domain (Figure S7B).

Unlike the well-studied voltage sensing domain in the Kv channels (Swartz, 2008), prestin lacks an extensively charged region in the membrane-embedded region (Figure S7E) and a great deal of effort has been focused on uncovering the prestin voltage-sensing region (Bai et al., 2006; Bai et al., 2009; Gorbunov et al., 2014; Homma et al., 2013; Oliver et al., 2001; Schaechinger et al., 2011; Takahashi et al., 2016; Tan et al., 2012). Mapping the host of residues that affect prestin NLC onto the structure shows that they are spread throughout the amino acid sequence and the 3D structure (Figure 1B, Figure S7F). Thus while some of these residues may not be involved in voltage sensing, but rather in anion binding or in structural transitions, it is clear that residues central to prestin's electromotive function are not localized to a specific region of the structure.

Chloride defines the anion binding site within the TMD

Anions, particularly chloride, are essential for the prestin eM function, proposed either to work as an extrinsic voltage sensor (Oliver et al., 2001) or to play an allosteric role (Rybalchenko and Santos-Sacchi, 2003). However, where anions bind to prestin has been elusive. Membrane proteins with a similar membrane topology, such as UraA (Lu et al., 2011) and UapA (Alguel et al., 2016) transporters, harbor their substrate binding sites at the cleft between TMs 3 and 10 in the central cavity at the core-gate domain interface. In the prestin structure, the equivalent site is surrounded by a positively charged yet partially hydrophobic pocket and is occupied by a chloride ion (Figure 2A, 2C), whose stable binding was confirmed by molecular dynamics (MD) simulations over the course of 1.5 μs (Figure S8A).

The residues that compose the anion binding site (Figure 2E) play key roles in prestin function (Gorbunov et al., 2014; Schaechinger et al., 2011). R399, the only positively charged residue close to chloride, stabilizes the nearby residues through interactions with

the side chains of N97 and S396 without direct interactions with chloride. Mutation of R399 to cysteine, glutamine or glutamate abolishes the NLC, while R399S positively shifts the voltage at peak capacitance (V_h) and abrogates salicylate inhibition (Gorbunov et al., 2014). The side chains of N97, S396 and S398 directly interact with chloride, consistent with the strong impact of the S398C mutation on anion interaction (Gorbunov et al., 2014). Three hydrophobic residues, L93, F101, and P136, give the anion binding site a partially hydrophobic character. Mutation of each of these residues individually shifts the V_h towards depolarization voltages, while the triple mutant abolishes the NLC in the physiological voltage range (Schaechinger et al., 2011). Taken together, these studies in the context of the prestin structure illustrate that anion binding is critical for prestin's eM function.

Salicylate binds to the anion site

Salicylate inhibits prestin and OHC function in a Cl^- dependent manner (Santos-Sacchi et al., 2006) and putatively locks prestin in an expanded state (Homma and Dallos, 2011; Santos-Sacchi and Song, 2014).

Replacing intracellular Cl^- with sulfate substantially shifts the NLC of OHCs (V_h) towards positive membrane potential (Muallem and Ashmore, 2006; Rybalchenko and Santos-Sacchi, 2008b). We performed NLC measurement with the HEK cells expressing prestin using sulfate internal buffer (without Cl^-) and observed a similar positive shift of V_h as sulfate replaces intracellular Cl^- (Figure S1F). These NLC curves, in the presence of intracellular Cl^- or sulfate, suggest that prestin likely forms a contracted state with chloride and an expanded state with sulfate at 0 mV membrane potential. To investigate the mechanisms underlying salicylate inhibition and structural transitions, we thus replaced chloride with sulfate and determined the structures of prestin either in the presence of 10 mM salicylate (termed Pres-Sal) or without salicylate (termed Pres-sulfate) at resolutions of 3.4 Å and 4.3 Å, respectively (Figures S2G–S2H, S4, S9). Because Pres-Sal and Pres-sulfate have similar structures (Cα RMSD: 0.57, Figure S11M) and Pres-Sal is of higher resolution, we use Pres-Sal structure for comparison with Pres-Cl if not otherwise mentioned (Cα RMSD: 1.45, Figure S11A). In the Pres-Sal structure, we observed an oval-shaped density at a similar position as Cl^- in Pres-Cl, showing how salicylate not only occupies the anion binding site but also physically overlaps with the Cl- ion position derived from the Pres-Cl structure (Figure 2B, 2D, 2F). To rigorously assess the binding and pose of salicylate to the anion site, we fit salicylate in the Pres-Sal map and performed MD simulations (Figure S8C). Salicylate remains stably bound at this site during MD simulations over the course of 250 ns, as assessed by the small fluctuations in its position and orientation (<=0.5 A displacement and =< 20° in orientation). In the resulting pose, the carboxylic group of salicylate is at a similar position of chloride and the binding of salicylate involves the same residues as chloride, with the aromatic ring projecting towards the core-gate domain interface. To experimentally verify this pose, we made modifications to prestin and salicylate and tested their effect on NLC. First, we reasoned that the binding site had additional space at the core-gate domain interface that should accommodate an even larger ligand. Indeed, we found that 10 mM 5-methylsalicylate inhibits the NLC of prestin similar to salicylate (Figure 2G–H, Figure S1E, S1G). We furthermore reasoned that the key interaction of F101 and salicylate should not be able to accommodate any additional groups (Figure 2G). We

therefore measured the NLC of the F101Y mutant and its inhibition by salicylate. The V_h of F101Y mutant is positively shifted from −54.0 ± 3.2 mV to 5.7 ± 1.9 mV (Figure S2F), consistent with previous studies (Schaechinger et al., 2011), and most importantly the inhibition by salicylate is diminished (Figure 2H, Figure S1F–S1G). Together, the observed electron density, MD simulation, and electrophysiology experiments prove that salicylate binds to the central anion binding side.

We were unable to locate sulfate in the electron-density map of Pres-sulfate. However, this could be due to the lower resolution of Pres-sulfate and does not exclude that sulfate can bind to the central anion site. We reasoned that if sulfate binds to the central anion site the F101Y mutant might change the effect of sulfate on the NLC of mutant. In the F101Y mutant we observed a similar shift to positive potentials than in the WT (Figure S1I), indicating the mutation did not affect sulfates interaction with prestin. In addition, we performed MD simulations to estimate the binding free energy of sulfate compared with chloride and salicylate. The MD simulation results suggest the binding of sulfate is weaker than Cl^- and salicylate (unbinding free energy, salicylate > Cl^- > sulfate) (Figure S8D, S8E). In summary, we cannot exclude that sulfate binds to the anion binding site but its binding affinity is probably substantially lower.

Anions populate distinct TMD conformations

The anion binding pockets in the Pres-Sal or Pres-sulfate structures are larger than that in the Pres-Cl structure, demonstrating that different anions result in distinct conformational states within the TMD (Figure S10). To assess these conformational differences, we examined structural changes relative to the anion binding site between the Pres-Cl and Pres-Sal structures (Figure 3A–3C). When superimposing the core domain, the gate domain undergoes a 4.6° rigid-body rotation (Figure 3A, Figure S11). Viewed from the extracellular side, the core and gate domains of Pres-Sal are more separated, resulting in a “swelling” of the TMD (Figure 3B). We measured the distances between the anion binding site and each helix in the gate domain, with all the distances measured in the Pres-Sal structure being larger than those in the Pres-Cl structure (Figure 3C). TMs 5 and 12, which are the helices near the anion binding site, have substantial distance changes in accordance with the larger substrate binding pocket observed in the Pres-Sal structure. Thus the TMD in the salicylate bound state is more expanded than that in the Cl^- bound state.

Prestin is a member of the SLC26 anion transporter family and thus we sought to relate the conformational states of prestin to those observed for the related anion exchanger 1 (AE1) in an outward-facing conformation (Arakawa et al., 2015), and SLC26A9 in an inward-facing conformation (Chi et al., 2020) (Figure 3D–3F). While in the AE1 and SLC26A9 structures no bound anion could be resolved their structures were consistent with anion binding in the same pocket formed by TM3 and TM10 as in prestin and involve the corresponding residues. The positions of the anion/substrate binding sites in prestin and these related transporters differ in their locations across the membrane. In AE1 the substrate binding site is closest to extracellular side, in SLC26A9 the anion binding site is closest to cytoplasmic side while in prestin structures they are in the middle. Among the prestin structures, the more expanded Pres-Sal or Pres-sulfate structure harbors the anion binding

site closer to the cytoplasmic side than the contracted Pres-Cl structure, suggesting the more expanded conformation of prestin is closer to an inward-facing conformation. Together with the solvent accessibility analysis (Figure S10), we conclude that the Pres-Cl and Pres-Sal/Pres-sulfate structures are best described as intermediate occluded-like states. Because intracellular anions can access the anion binding site under physiological conditions (Oliver et al., 2001) and chloride ions were observed to un- and re-bind in our MD simulations (Figure S8A, S8B), thermal fluctuation of the intracellular gate may allow exchange of anions in the occluded-like states.

Salicylate stabilizes an expanded state

To understand how the binding of different anions affects the prestin dimer conformation and thus the nearby membrane, we aligned the Pres-Cl and Pres-Sal structures using the structurally invariant STAS domain dimer (Figure 4A, 4B, Figure S11, Movie S1). This superimposition revealed that a substantial proportion of conformational differences between the two states can be understood as a rigid-body movement between the core, gate, and STAS domain (Figure S11). The gate and the core domain rotate 5–6° around two different axes that are at a 45° angle to the membrane bilayer, but roughly perpendicular to each other. The result of these movements is a shift of TMs 2, 9, and 11 of the core domain and TMs 5b, 6, and 7 of the gate domains away from the center of the TMD (Figure 4A), resulting in an expansion of the TMD (Movie S1). Nevertheless, the gap between the ‘V’ shaped, separated TMDs remains almost unchanged, with the two cholesterol-like molecules bound to similar positions in Pres-Cl and Pres-Sal (Figure S14C–E).

To quantify the expansion, we calculated the cross-sectional area of prestin, perpendicular to the two-fold axis, using a Gaussian map calculated from the model coordinates (Figure 4C). In the TMD, Pres-Sal has a consistently increased cross-sectional area. Averaged over the transmembrane area the difference between the cross-section of Pres-Cl and Pres-Sal is about 200 $Å^2$. While the measured cross-section depends on an arbitrarily chosen threshold, the difference is constant across a range of thresholds (Figure S12C–S12E). Furthermore, the cross-sections of Pres-Cl and Pres-Sal are similar within the cytosolic domain. We performed a similar analysis on the Pres-sulfate structure and found that it was also expanded compared to Pres-Cl (Figure S12A, S12B). While Pres-sulfate has a slightly higher cross-section than Pres-Sal the biological significance of this is unclear due to the coordinate uncertainty resulting from the low resolution of Pres-sulfate. We note that this expansion will only be effectively transduced to the membrane if the overall orientation of the TMD remains unchanged, which provides an explanation for why prestin is a dimer and for the important role of the STAS domain. The magnitude of the cross-section increase, roughly 5% of the total cross-section area, is consistent with estimates of the electromotive change in OHC (Ashmore, 2019).

To further examine the effect of prestin structural transition between the expanded and contracted form on the membrane bilayer, we performed simulations of membrane-embedded prestin, during which the protein was steered to switch its conformation from the contracted state in the presence of chloride to the expanded state in the presence of salicylate using a time-dependent force protocol (Supplemental Information, Figure S12F,

S12G). Two independent simulations probed the structural changes in opposite directions, one examining the effect of prestin expansion, and the other probing the effect of the protein contraction. These simulations capture the response of the membrane to the proteins conformational changes in a consistent manner to our structural interpretation of the cryoEM results, namely, membrane expansion due to transition of prestin from a contracted to an expanded state, and membrane shrinking due to the opposite structural change of prestin.

Most models of prestin function assume that its expansion is coupled to the movement of a charged voltage sensor across the lipid membrane. There is no consensus on whether this voltage sensor charge consists of the bound chloride (extrinsic voltage sensor) or of charged residues within prestin (intrinsic voltage sensor) (Bai et al., 2009; Oliver et al., 2001). To address this question, we asked whether the anion binding site moves across the membrane between contracted (Pres-Cl) and expanded (Pres-Sal) states. Because we cannot measure movement of the anion directly, we analyzed the movement of four residues surrounding the binding pocket: S398, Q97, A138, and V353 (Figure 4D, 4E). We found that Cα atoms of these residues were shifted towards the intracellular side in the Pres-Sal structure compared to the Pres-Cl structure by 1.5, 1.0, 1.7, and 2.0 Å, respectively. In the case of the extrinsic voltage sensor model, one would expect a movement of the anion binding side towards the extracellular side going from the contracted conformation at depolarized potentials to the expanded state at hyperpolarized potentials (Rybalchenko and Santos-Sacchi, 2008a). Furthermore, the valence of the charge movement parameter z in the two-state Boltzmann model used to fit NLC measurements (see Methods) is 0.64, indicating that in case of a single moving charge with a valence of 1, one would expect it to move 0.64 times the span of the membrane (~25 Å). Since we observe in our structures an opposite movement that is an order of magnitude shorter, our data are more consistent with the intrinsic voltage sensor model, where partial charges of multiple sidechains distributed within prestin move by smaller amounts so that the sum of these charge movements adds up to 0.64. While we do observe charged residues moving perpendicular to the membrane (Figure S13), we do not find a consistent pattern of charge movement that would explain the NLC, suggesting that changes in the polarization of the membrane causes additional conformational changes compared to the exchange of chloride and salicylate.

Prestin deforms the lipid bilayer

Prestin is sensitive to changes in membrane tension (Santos-Sacchi et al., 2001; Santos-Sacchi and Tan, 2020) and thickness (Fang et al., 2010), as well as cholesterol concentration (Kamar et al., 2012). In investigating the interactions of lipids with our structures we found that the resolved lipids were not arranged in a plane perpendicular to the two-fold axis (Figure 5A–5C, Figure S14A, S14B). At the lateral interface between the core and gate domains, lipid molecules were displaced towards the extracellular side while lipids found between the transmembrane domains of the two protomers were displaced towards the intracellular side. The deformation of the lipids from a plane is also mirrored in the estimated lipophilicity of the surface of prestin and causes a “saddle”-shaped micelle and nanodisc density (Figures S3, S4). The distance along the two-fold axis between lipids displaced the furthest towards the extracellular or cytosolic side is around 15 Å.

To confirm that insertion of prestin into a lipid bilayer would result in significant deformation of the surrounding lipid bilayer we analyzed 1.5 μs-long MD simulation trajectories of membrane-embedded prestin, both in the Cl^--bound form and in the salicylate-bound conformation (Supplemental Information). For the equilibrated protein-membrane system, the lipids in the outer leaflet are found to be depressed in the area between the TMDs by ~7.5 Å (relative to the bulk average height of lipids) and elevated at the lateral gate/core interface by ~7.5 Å (Figure 5E), resulting in an overall ~15 Å deformation of lipids at the protein interface (Figure 5A, 5E). At the lower leaflet lipids at the lateral core-gate domain interface are similarly moved towards the extracellular side by ~7.5 Å (Figure 5D). Together these results suggest that prestin profoundly alters the shape of its surrounding lipid bilayer. The membrane deformation is reminiscent of the mechanically-gated piezo channels (Ge et al., 2015; Guo and MacKinnon, 2017; Saotome et al., 2018), although smaller in scale. It has been proposed that in piezo channels “flattening” of the membrane due to membrane tension stabilizes the open state (Guo and MacKinnon, 2017). In prestin increasing membrane tension shifts the voltage of peak capacitance in the positive direction (Santos-Sacchi et al., 2001; Santos-Sacchi and Tan, 2020), which could be explained by selective stabilization of the expanded state due to membrane ‘flattening’.

Mechanism underlying electromotility

Binding of anions to a binding pocket within the TMD of each prestin protomer modulates the conformation of the TMD (Fig. 6). In the absence of chloride and in the presence of salicylate, a rigid-body motion between core and gate domains results in a swelling of the TMD, consistent with the ‘area-motor’ model (Iwasa, 1994). We hypothesize that the conformational changes between the contracted and expanded states, visualized here, provide important clues to the motions of prestin evoked by changes in membrane potential. To our knowledge this is a previously unseen mechanism for a molecular motor and provides a structural framework for the transduction of electrical signals into mechanical motion. The fact that prestin is contracted in the presence of chloride and that the anion binding site moves toward the intracellular side in the expanded state rules out chloride as an extrinsic voltage sensor. More likely, multiple residues previously identified as involved in NLC function and shown here to be distributed at the intracellular and extracellular membrane interfaces form an intrinsic voltage sensor. Our structures indicate that salicylate inhibits eM by displacing chloride from the anion-binding site and by preventing the structural transitions to contracted state. An unexpected finding of profound membrane distortion by the prestin dimer, together with specifically bound cholesterol molecules between the TMDs, raise the importance of lipid interactions for prestin function and provide a structural rationale for the influence of cholesterol, membrane tension, and membrane thickness on prestin function.

STAR★METHODS

CONTACT FOR REAGENT AND RESOURCE SHARING

Requests for reagents may be directed to the Lead Contact, Eric Gouaux (gouauxe@ohsu.edu).

EXPERIMENTAL MODEL AND SUBJECT DETAILS

Construct and cell culture—The gene encoding full-length human prestin (Uniprot ID: P58743–1) was synthesized and subcloned into the pEG BacMam vector (Goehring et al., 2014). The construct contains a C-terminal 3C protease cleavage site, an enhanced green fluorescent protein (eGFP), and a StrepII tag. Sf9 cells (ThermoFisher 12659017) were used for BacMam virus amplification and were cultured in Sf-900 III SFM medium at 27 °C. To express prestin for structural studies and functional analysis, HEK293 GnTI$^-$ cells were cultured in suspension using FreeStyle medium supplemented with 2% (v/v) fetal bovine serum at 37 °C. Both cell lines are routinely tested for mycoplasma contamination using CELLshipper Mycoplasma Detection Kit M-100 from Bionique and are mycoplasma free. No misidentified cell lines were used.

Prestin expression and purification—HEK293 GnTI$^-$ cells cultured at 37°C with a density of ~2.5 × 10^6 ml$^-$ were infected with prestin BacMam virus at an MOI of 1:1. A final concentration of 10 mM sodium butyrate was added 12 hours after infection, and cells were cultured at 37°C for another 48 hours. Cells were harvested and lysed in buffer containing 20 mM Tris pH 8.0, 150 mM NaCl, 2% (w/v) digitonin, and protease inhibitors (1 mM phenylmethylsulfonyl fluoride, 0.8 μM aprotinin, 2 μg/ml leupeptin and 2 μM pepstatin A) for three hours at 4 °C. The insoluble material was removed by centrifugation at 186,009 *g* for one hour. The supernatant was filtered through a 0.45 um filter and incubated with Strep-Tactin resin, washed with 20 mM Tris HCl pH 8.0, 150 mM NaCl, 0.02% (w/v) glycol-diosgenin (GDN), 0.004% (w/v) CHS, and eluted with the same buffer supplemented with 5 mM desthiobiotin. The eluate was concentrated and treated with 1:100 (w/w) 3C protease to remove the C-terminal GFP for 2 hours at 4°C. For prestin bound with chloride (Pres-Cl), the concentrate was loaded onto a size-exclusion chromatography (SEC) column (Superose 6 Increase 10/300 GL) equilibrated in a buffer containing 20 mM Tris HCl pH 8.0, 150 mM NaCl, 0.02% GDN. For prestin in the presence of sulfate and the absence of chloride (Pres-sulfate), an SEC buffer containing 20 mM Tris sulfate pH 8.0, 60 mM Na_2SO_4, 0.02% GDN was used to replace the chloride. Peak fractions from both conditions were pooled and concentrated for cryo-EM grid preparation. For the salicylate-bound state (Pres-Sal), the concentrated Pres-sulfate sample was incubated with a final concentration of 10 mM sodium salicylate for 10 minutes before cryo-EM grid preparation.

For prestin in lipid nanodisc (Pres-Cl-nanodisc), porcine brain total lipid extract was dissolved in chloroform, dried in a rotary evaporator, and kept in a vacuum chamber overnight. The lipids were rehydrated to a final concentration of 20 mM with buffer containing 20 mM Tris pH 8.0 and 150 mM NaCl by several freeze-thaw cycles. MSP1E3D1 scaffolding protein, which yields nanodiscs with an estimated outer membrane diameter of ~12 nm, was purified as previously described (Alvarez et al., 2010). The lipid suspension was dissolved with a final concentration of 1% (w/v) GDN and 0.2% (w/v) CHS for 30 min and then incubated with prestin and MSP1E3D1 for 1 hour with a molar ratio of 1:5:600 (prestin dimer: MSP: lipid). Three batches of biobeads were added for detergent removal and nanodisc formation at 4 °C, with the first two batches incubating for 2 hours and the last one overnight. For proteolysis, 3C protease (1:100 w/w) was combined with the last batch of biobeads to remove the GFP. The material was further purified by SEC

(Superose 6 Increase 10/300 GL column) with a buffer containing 20 mM Tris-HCl pH 8.0 and 150 mM NaCl. Peak fractions were harvested and concentrated for cryo-EM grid preparation.

Cryo-EM grid preparation and data collection—Aliquots of prestin (3.5 ul at ~3 mg/ml) in either detergent micelles or lipid nanodiscs were applied onto Quantifoil holey carbon grids (R2/2, 200 mesh, gold) that had been glow discharged at 15 mA for 60 s. The grids were blotted with a Vitrobot mark IV at 100% humidity using a blotting time of 4s and a blotting force of 0 at 8 °C. The grids were plunge-frozen into liquid ethane cooled by liquid nitrogen.

Micrographs were collected on 300 kV Titan Krios electron microscopes equipped with an energy filter and a Gatan K3 camera. SerialEM (Mastronarde, 2005) was used for automated data collection. Data collection for all datasets followed a similar strategy with a total dose of 50 e^{-}/Å, 50 frames, and a defocus range of −0.8 to −2.5 μm. The Pres-Cl and Pres-Cl-nanodisc datasets were collected with a dose rate of 18 e/pix/s and a pixel size of 0.651 Å/pixel without the correlated double sampling (CDS) mode. The Pres-Sal and Pres-sulfate datasets were collected with the CDS mode, a dose rate of 4.5 e/pix/s, and a pixel size of 0.676 Å/pixel. The data collection statistics are summarized in Table S1.

Image processing—Raw micrographs in super-resolution mode were binned by 2x and corrected for both full-frame and local motion with the patch motion correction in cryoSPARC (Punjani et al., 2017; Rubinstein and Brubaker, 2015). Contrast transfer function (CTF) parameters were estimated with patch CTF estimation in cryoSPARC. Particles were initially picked from a small fraction of the Pres-Cl dataset with Gaussian blob picking and subjected to 2D classification. Class averages showing reasonable prestin features in various orientations were selected as templates for template-based particle picking. Particles from these class averages generated an *ab initio* model in cryoSPARC. For each full dataset, extracted particles were down-sampled by two times to either 1.301 Å (Pres-Cl and Pres-Cl-nanodisc) or 1.352 Å (Pres-Sal or Pres-sulfate), followed by one round of 2D classification to remove ‘junk’ particles.

For the Pres-Cl dataset, 3D classification into eight classes with the *ab initio* model as a reference was performed using either C1 or C2 symmetry. Both symmetries resulted in one good class out of eight with apparent C2 symmetry, indistinguishable structural features, and similar particle distribution. Therefore, C2 symmetry was used for subsequent image processing. 3D refinement with the bin-2 particles from the single good class resulted in a reconstruction at an overall resolution of 2.71 Å. Particles were re-extracted with the bin-1 pixel size of 0.651 Å and a box size of 512 pixels. 3D refinement with the re-extracted particles resulted in a reconstruction at 2.46 Å resolution. One more round of 3D classification and multiple rounds of local CTF refinement and non-uniform (NU) refinement (Punjani et al., 2019) were performed using cryoSPARC, improving the resolution to 2.34 Å. The particle stack was further subjected to one round of 3D classification without alignment in RELION 3.1 and reconstructed using NU refinement in cryoSPARC, resulting in a 2.31 Å resolution reconstruction. Detailed data processing of Pres-Cl dataset can be found in Figure S3.

For Pres-Cl-Nanodisc and Pres-Sal datasets, the same data processing strategies were used except that no 3D classification step in RELION was performed, resulting in reconstructions at resolutions of 2.70 Å and 3.43 Å, respectively.

For the Pres-sulfate dataset, bin-2 (1.352 Å/pix) particles after 2D classification in cryoSPARC were exported to RELION 3.1 for global 3D classification into eight classes. One out of the eight classes had promising prestin features. Refinement of the single class resulted in a 7 Å resolution reconstruction in RELION 3.1. One round of local 3D classification followed by refinement of the best class further improved the resolution to 5.2 Å. After bin-1 (0.676 Å/pix) particles were re-extracted, a reconstruction at ~5 Å resolution was obtained from RELION 3.1. The particles were moved to cryoSPARC for one round of homogeneous refinement and multiple rounds of local CTF refinement and NU refinement, improving the reconstruction to ~4.3 Å. Detailed data processing of Pres-sulfate dataset can be found in Figure S9.

The resolutions were estimated by FSC = 0.143, calculated by both half maps with a soft solvent mask in cryoSPARC. The angular distribution of particles was plotted with the python script star2bild.py in the UCSF pyem package (Asarnow, 2019). The local resolution was calculated in cryoSPARC. Detailed data processing statistics and map quantifications are listed in Table S1, Figure S4.

Structure determination and model building—The 2.3 Å resolution cryo-EM map of Pres-Cl allows for *de novo* model building with high confidence in COOT (Emsley et al., 2010). Most regions are well resolved with clear side chain features for residue registration. The N-terminal 1–11 residues and C-terminal 726–744 residues could not be built due to the lack of density in the map. We built a ~50 amino acid stretch of the intervening sequence (IVS) region (~80 residues in total), which was previously considered unstructured and flexible. The first part of the IVS (residues 561–580) forms the Cα2 helix with residues 564–580. The second part of the IVS (residues 614–640) was built based on the unique side chain features of residues 616–622 (YPPIVIK), which also helped to determine the loop orientation and the location of the remaining residues. In the extracellular loop region, residues 162–166 were less well resolved and poly-alanines were built. Lipid-like densities were fitted with alkanes with various number of carbons. Solvent-like densities were modeled with water molecules that were automatically added by Phenix (version 1.19rc5–4047) (Liebschner et al., 2019) and inspected in COOT. The model was refined in real space with Phenix (version 1.18.2–3874).

For model building of the other structures, the Pres-Cl structure without lipids and waters was fit into cryo-EM maps in ChimeraX (Pettersen et al., 2020) and adjusted in COOT. For Pres-Cl-Nanodisc, the chloride was built similarly to Pres-Cl. For Pres-Sal, the salicylate was fit into the oval shape of density that appeared in a similar position as the chloride anion in Pres-Cl. The orientation of salicylate was determined by the density features, the surrounding residues and the molecular dynamics simulation (Supplemental Information). All final models were subjected to real-space refinement and validated in Phenix (version 1.18.2–3874). Map and structure figures were generated using Pymol or ChimeraX.

Electrophysiology—HEK293 GnTI$^-$ cells were transfected with the construct (pEG Bacmam CMV-hPrestin-GFP) for the cryo-EM studies and used for recordings 24–48 h after transfection. The recording pipettes had resistances of 2.5–3.5 MΩ when filled with the Cl^- internal solution containing (in millimolar) 135 CsCl, 5 $MgCl_2$, 2 Na_2ATP, 10 HEPES and 10 EGTA or with the SO_4^{2-} internal solution containing (in millimolar) 88 Na2SO4, 2 MgSO4, 10 HEPES, 3 MgATP, and 10 EGTA (pH adjusted to 7.35). Cells with a membrane resistance greater than 500 MΩ after rupturing were recorded in a bath filled with external solution containing (in millimolar) 120 NaCl, 2 $CoCl_2$, 1 $CaCl_2$, 2 $MgCl_2$, 20 TEACl, 10 HEPES (pH adjusted to 7.35). Recordings are performed with Cl^- internal buffer if not otherwise mentioned. All solutions were adjusted to 310 ± 2 mOsm/L. For salicylate and 5-methylsalicylate inhibition experiments, 10 mM salicylate or 10 mM 5-methylsalicylate was added to the external solution (adjusted to pH 7.35, 310±2 mOsm/L).

For NLC measurement with the “Sine+DC” method, HEK cells on coverslips were mounted on an upright microscope (BX51WI, Olympus) and viewed at 60x magnification using direct interference contrast (DIC). Transfected cells were identified using epifluorescence (Filter wavelength). Images were acquired with an ORCA Flash 4.0LT CMOS camera operated with CellSens software (Olympus). Lockin C_m measurements were performed using an EPC10 amplifier and Patchmaster software (HEKA; Germany). Voltage-clamp C_m recordings were done with a sinusoidal wave (2khz; 30mV peak-to peak) superimposed on holding potential (0 mV). Incremental voltage steps were given from −150mV (dV=10mV; 200ms). C_m traces were analyzed and plotted in IgorPro software (Wavemetrics, Lake Oswego). C_m was measured by averaging the last 150ms of each voltage step.

For NLC measurement with the dual-sine methodology, recordings were carried out at room temperature under the whole-cell patch clamp mode using an Axopatch 200A amplifier. Cells were placed in either external solution only or external solution supplemented with 10 mM salicylate (or salicylate analogs) for 2 min before each recording. Whole-cell capacitance was measured at 0 mV holding potential using a two sine wave voltage stimulus protocol (10 mV amplitude at both 390.6 and 781.2 Hz), followed by the fast Fourier transform-based admittance analysis using jClamp (www.scisoftco.com). Series resistance was compensated before recording and the residual was corrected with the built-in function in jClamp. The voltage-dependent capacitance was fit with the first derivative of the two-state Boltzmann function:

$$C_m = \frac{Q_{max}\left(\frac{ze}{kT}\right)}{\exp\left(\frac{ze}{kT}\left(V_m - V_h\right)\right) \times \left(1 + \exp\left(\frac{ze}{kT}\left(V_m - V_h\right)\right)\right)^2} + C_{lin}$$

Where Q_{max} is the maximum charge transfer, z is the valence of charge movement, e is electron charge, k is the Boltzmann’s constant, T is the absolute temperature, V_m is the membrane potential, V_h is the voltage at peak capacitance, C_{lin} is the linear capacitance. The fitted parameters for prestin WT and F101Y mutant are as follows: Q_{max} = 0.112 ± 0.009 pC, z = 0.64 ± 0.02; V_h = −54.0 ± 3.2 mV, C_{lin}= 10.94 ± 0.75 pF, Q_{max}/C_{lin} = 10.7 ± 1.1 fC/pF for WT (n=14), and Q_{max} = 0.066 ± 0.008 pC, z= 0.63 ± 0.02; V_h = 5.7 ± 1.9 mV,

C_{lin}= 7.98 ± 0.43 pF, Q_{max}/C_{lin} = 8.6 ± 1.1 fC/pF for F101Y (n=20). Data are presented as means ± standard errors of means.

Computational Methods

System preparation: Cl^--, salicylate-, and sulfate-bound prestin cryo-EM structures were prepared for molecular dynamics (MD) simulations following the procedures described below. Missing side chains and hydrogen atoms were added to the experimental, cryo-EM models, using the PSFGEN plugin (https://www.ks.uiuc.edu/Research/vmd/plugins/psfgen/) in VMD (Humphrey et al., 1996). The experimental models are missing a disordered region in the intracellular domain, dividing the structures into two polypeptide segments (residues 13–580 and 614–724, respectively). Neutral N-terminal and C-terminal 'caps' were added to the first and last residues of each polypeptide segment, respectively, using PSFGEN. The coordinates of the bound Cl^- and sulfate ions were based on the modeled Cl^- in the cryo-EM structure, whereas the bound salicylate was placed in the binding pocket using our in-house docking protocol, GOLEM (see 'Computational search for docking poses of salicylate' for more details). Following pKa estimation by PROPKA (Olsson et al., 2011; Sondergaard et al., 2011), all titratable residues were modeled in their default titration states, which was modeled in its protonated (neutral) form. All protein structures were internally hydrated using the DOWSER (Gumbart et al., 2009; Zhang and Hermans, 1996) plugin of VMD. The two cholesterol molecules modeled in the experimental structures were included in the Cl^-- and salicylate-bound systems. The lipid bilayer used to embed the proteins was constructed in CHARMM-GUI (Jo et al., 2008). The orientation of the protein in the bilayer was obtained from the OPM (Orientations of Proteins in Membranes) database (Lomize et al., 2006). The protein, along with the bound cholesterol molecules, was then inserted into a heterogeneous lipid bilayer, followed by removing sterically clashing lipid molecules. The bilayer is composed of palmitoyl-oleoyl-phosphatidyl-choline (POPC), palmitoyl-oleoyl-phosphatidyl-ethanolamine (POPE), palmitoyl-oleoyl-phosphatidyl-glycerol (POPG), palmitoyl-oleoyl-phosphatidyl-inositol (POPI), palmitoyl-sphingomyelin (PSM), and cholesterol (CHOL) lipids at a molar ratio of 32:16:5:11:16:20. The protein-membrane system was then solvated with water including 150 mM NaCl in VMD (system size: 335k atoms). To further reduce any bias from the initial lipid configuration and increase the sampling, two independent membrane systems (with randomly placed initial lipids) were generated for Cl^--bound prestin.

Computational search for docking poses of salicylate: The salicylate binding pose in our simulations was obtained using an in-house docking package called GOLEM (Zhao and Tajkhorshid, 2021) This software tool employs a genetic algorithm to explore a ligand's conformational, orientational, and positional space, with explicit consideration of water displacement, as well as bridging water molecules' position and orientation, to optimize the fitness, which is defined as the combination of the system's energy and fitting to the cryo-EM density. Despite the stochasticity of the genetic part of the algorithm, given the large number of iterations. GOLEM robustly reproduces the ligand's docked pose with negligible differences in repeated trials. The resulting docked pose can be further validated by equilibrium MD simulations, as done in this study.

Equilibrium molecular dynamics (MD) simulation: All MD simulations were performed using NAMD simulation package (Phillips et al., 2020) and employing the fully atomistic CHARMM36m (Huang et al., 2017) and CHARMM36 (Klauda et al., 2010) force fields for the protein and lipids, respectively. The TIP3 model was used for water molecules (Jorgensen et al., 1983). The salicylate was parameterized using the CHARMM general force field (CGenFF) webserver (https://cgenff.paramchem.org) (Vanommeslaeghe et al., 2010; Vanommeslaeghe et al., 2012) and further optimized employing the Force Field Toolkit (ffTK) plugin (Mayne et al., 2013) of VMD. Sulfate parameters were adopted from a previous study employing ab initio calculations (Cannon et al., 1994). A 12 Å cutoff was used for short-range, non-bonded interactions, with switching starting at 10 Å. Long-range electrostatic interactions were calculated using the particle mesh Ewald (PME) algorithm (Darden et al., 1993) with a grid density of 1 $Å^{-1}$, and a PME interpolation order of 6. All bonds involving hydrogen atoms were kept rigid using the SHAKE algorithm (Ryckaert et al., 1977). Temperature was maintained at 310 K using Langevin thermostat with a damping coefficient of 1.0 ps^{-1}. Pressure was maintained at 1 atm by the Nosé-Hoover Langevin piston barostat (Feller et al., 1995; Martyna et al., 1994), with period and decay of 100 and 50 fs, respectively. All systems were simulated in a flexible cell allowing the dimensions of the periodic cell to change independently while keeping the cell aspect ratio in the *xy* plane (membrane plane) constant. The simulation timestep was set to 2 fs. Lennard-Jones and PME forces were updated at one and two timesteps, respectively. Atomic coordinates were saved every 10 ps.

The two Cl^--bound systems were simulated using the following steps: (**1**) 10,000 steps of minimization, followed by 5 ns equilibration, in which harmonic position restraints (k = 10 kcal.mol^{-1}.$Å^{-2}$) were applied to the position of protein's heavy atoms modeled in the cryo-EM structure, as well as to the heavy atoms of the two modeled cholesterol molecules and the bound Cl^- ions. Furthermore, the z position (normal to the membrane plane) of phosphorus atoms in phospholipids and oxygen atoms of bulk cholesterols were also restrained in this step using a harmonic potential (k = 5 kcal.mol^{-1}.$Å^{-2}$); (**2**) 20 ns of equilibration with only the protein backbone, heavy atoms of the two modeled cholesterol molecules, and the bound Cl^- ions restrained harmonically (k = 10 kcal.mol^{-1}.$Å^{-2}$); (**3**) 5 ns of equilibration in which all the restraints from the previous step were removed by decreasing the force constant stepwise from 10 to 0 kcal.mol^{-1}.$Å^{-2}$; (**4**) production equilibrium runs for 1.5 μs without any restraints.

The simulation of the salicylate-bound system was performed to check the stability of the docked pose of the inhibitor, and therefore, followed a different protocol: (**1**) 10,000 steps of minimization, followed by 5 ns of equilibration with harmonic restraints (k = 10 kcal.mol^{-1}.$Å^{-2}$) on the all the protein's heavy atoms modeled in the cryo-EM structure, and on the heavy atoms of the bound salicylates, water molecules placed close to the salicylates by the the docking protocol, the two modeled cholesterols. In addition, z positional restraints were applied (k = 5 kcal.mol^{-1}.$Å^{-2}$) to phosphorus atoms of phospholipids and oxygen atoms of bulk cholesterols; (**2**) 20 ns of equilibration in which the protein backbone atoms were restrained (k = 10 kcal.mol^{-1}.$Å^{-2}$), while the salicylate and protein side chains were free to move; (**3**) production run extending the simulation in Step **2** to 250 ns.

The simulation of sulfate-bound structure was conducted to obtain an equilibrated system for free energy perturbation (FEP) simulations used to calculate the binding affinity of sulfate in the binding pocket, and therefore, followed a shorter protocol: (**1**) 10,000 steps of minimization, followed by 5 ns equilibration, while applying harmonic position restraints (k = 10 kcal.mol^{-1}.Å^{-2}) to the protein's heavy atoms modeled in the cryo-EM structure, and to the modeled sulfate ions in the binding pockets. Furthermore, the z position of phosphorus and oxygen atoms in phospholipids and cholesterols were also harmonically restrained, respectively (k = 5 kcal.mol^{-1}.Å^{-2}); (**2**) 20 ns of equilibration with the protein backbone, and bound sulfate ions restrained harmonically (k = 10 kcal.mol^{-1}.Å^{-2}).

Prestin conformational transition between the states: Two non-equilibrium MD simulations were performed to drive transitions between the contracted and expanded states and to monitor the response of the membrane to these transitions, one in the forward (contracted to expanded) and one in the backward (expanded to contracted) direction. The Cl^--bound cryo-EM structure represented the contracted state, while the salicylate-bound conformation was used to represent prestin in its expanded state. The same protocol as described in **'System preparation'** was employed to construct the contracted and expanded systems. Since the goal was to investigate the coupling between the protein's conformational transitions and the membrane, we did not include the bound Cl^- and salicylate in these simulations.

These transition simulations follow the same driving protocols (but in opposite directions): **(1)** 10,000 steps of minimization, followed by 5 ns equilibration while restraining the protein's heavy atoms modeled in the cryo-EM structure, as well as the heavy atoms of the two modeled cholesterol molecules, using a harmonic potential (k = 10 kcal.mol^{-1}.Å^{-2}). Moreover, harmonic z position restraints were applied to phosphorus and oxygen atoms of phospholipids and bulk cholesterols, respectively (k = 5 kcal.mol^{-1}.Å^{-2}); **(2)** 20 ns of equilibration with harmonic restraints on the protein backbone, as well as on the heavy atoms of the two modeled cholesterol molecules (k = 10 kcal.mol^{-1}.Å^{-2}); **(3)** keeping the same restraints only on the protein backbone and further equilibrating the system for 150 ns; **(4)** a 50 ns non-equilibrium simulation, with time-dependent biases applied to drive the conversion from the initial to the target state using the collective variables (colvars) module of NAMD (Fiorin et al., 2013). This transition was achieved by applying biasing forces (k = 1.5 kcal.mol^{-1}.Å^{-2}) on the protein C_α atoms to decrease their RMSD with respect to those in the target structure; **(5)** maintaining the protein in the target state for additional 150 ns by applying the final set of biases (not moving this time) introduced in step **(4)**.

During the transitions between the contracted and expanded forms (the non-equilibrium phase of the simulations in Step 3), the x and y dimensions of the simulation box (membrane dimensions) were recorded every 10 ps. The resulting xy plane area reflects the total cross-sectional area of the membrane-protein system.

Analysis of molecular dynamics trajectories: Molecular images from MD trajectories are generated with VMD (Humphrey et al., 1996). The membrane deformation induced by prestin is quantified by recording the z component of the center of mass of the lipids' phosphate (PO_4^-) groups during the last 500 ns of the Cl^--bound trajectories. The origin of

the *z* axis is defined as the bilayer midplane. The resulting heatmap (binned in 2×2 $Å^2$ bins) in each leaflet captures the spatial distribution of the height of the lipid head groups within the membrane.

The dynamics of the Cl^- ions at their binding sites were monitored by measuring their displacement from the original (experimentally modeled) positions. When analyzing Cl^- dynamics in each binding site, to average out the motion of the binding site itself, the trajectories were aligned using C_α atoms of the binding-site residues (Q97, F101, P136, F137, L397, S398, and R399) with respect to those in the cryo-EM structure. Then, the distance between the ion (either from the initial model or from the bulk solution) to the modeled Cl^- in the cryo-EM structure was recorded. The distance plots were smoothed using a sliding window of 1 ns.

The stability of the docked salicylate in the two subunits was monitored by calculating the displacement and change in the orientation of the ligand throughout the simulations. The displacement was obtained by calculating the center of mass displacement of salicylate from its docked pose in each frame of the trajectory. The orientational change was defined as the angular change of the normal vector to the salicylate's benzene ring plane with respect to that of the docked pose. Both the displacement and orientation plots were smoothed using a sliding window of 0.2 ns.

Free energy calculation of ligand binding affinity: FEP simulations (Cournia et al., 2017) were performed on the Cl--, salicylate-, and sulfate-bound structures to compare relative binding affinities of the three ligands. During the employed FEP protocol, the ligand is annihilated from the binding pocket of one prestin protomer while being created at a location in bulk solution 80 Å away from the binding pocket. The FEP calculations of Cl--, salicylate-, and sulfate-bound structures were initiated from the last frame of the Step 2 of the equilibration protocol (see Equilibrium molecular dynamics simulation for more details). During FEP calculations, the protein backbone heavy atoms were restrained (k = 10 kcal.mol-1.Å-2) to the corresponding experimentally modeled positions to avoid undesired structural deviations. All other simulation parameters were the same as in the aforementioned equilibrium simulations. The alchemical transformations were performed in both forward (λ increasing from 0 to 1; ligand annihilation in the binding site and creation in solution) and backward (λ decreasing from 1 to 0; ligand creation in the binding site and annihilation in solution) directions to assess the reversibility. A soft-core van der Waals radius-shifting coefficient of 5 Å was chosen. In the forward transformation, the vdW and electrostatic interactions of the annihilated particles were linearly decoupled to the simulation over a λ range of 0–1 and 0–0.5, respectively, whereas in the backward transformation these interactions were linearly coupled to the simulation in the corresponding λ range. Each FEP calculation along the λ reaction path was divided into 50 equally-spaced consecutive windows to ensure gradual transformation. Within each window, the performed simulation consisted of 5000 steps of minimization, an equilibration phase of 100 ps, followed by 1 ns simulation for data collection at the frequency of every 20 fs, resulting in an accumulated simulation time of 110 ns for each system. To prevent the dissociation of the ligand during the alchemical transformation, harmonic restraints were applied to the annihilated and created ligands (k = 10 kcal.mol-1.Å-2). All the simulations

were performed, employing the FEP module of NAMD (Chen et al., 2020). The outputs were analyzed using the ParseFEP (Liu et al., 2012) plugin in VMD, with the statistical error estimated using the implemented Bennett Acceptance Ratio (BAR) method (Bennett, 1976).

Supplementary Material

Refer to Web version on PubMed Central for supplementary material.

Acknowledgments

We would like to thank the staff at Pacific Northwest Cryo-EM Center (PNCC), OHSU MMC and Janelia Research Campus for the assistance in cryoEM data collection, and the staff at UW for the assistance in cryoEM preliminary screening. We thank L. Vaskalis for assistance with figures, H. Owen and R. Hallford for help with manuscript preparation and Gouaux lab members for discussions. The computational component of the project was supported by the National Institutes of Health (NIH) under award numbers P41-GM104601 (to ET), and R01-GM123455 (to ET). We also acknowledge computing resources provided by Blue Waters at National Center for Supercomputing Applications, Extreme Science and Engineering Discovery Environment (grant MCA06N060 to ET), and by Microsoft Azure. This work is also supported by NIH grants grants RO1 DC004274 and DC012938 to H.v.G. from National Institute on Deafness and Other Communication Disorders. E.G is an investigator of the Howard Hughes Medical Institute.

References

Afonine PV, Poon BK, Read RJ, Sobolev OV, Terwilliger TC, Urzhumtsev A, and Adams PD (2018). Real-space refinement in PHENIX for cryo-EM and crystallography. Acta Crystallogr D Struct Biol 74, 531–544. [PubMed: 29872004]

Alguel Y, Amillis S, Leung J, Lambrinidis G, Capaldi S, Scull NJ, Craven G, Iwata S, Armstrong A, Mikros E, et al. (2016). Structure of eukaryotic purine/H(+) symporter UapA suggests a role for homodimerization in transport activity. Nat Commun 7, 11336. [PubMed: 27088252]

Alvarez FJD, Orelle C, and Davidson AL (2010). Functional reconstitution of an ABC transporter in nanodiscs for use in electron paramagnetic resonance spectroscopy. Journal of the American Chemical Society 132, 9513–9515. [PubMed: 20578693]

Arakawa T, Kobayashi-Yurugi T, Alguel Y, Iwanari H, Hatae H, Iwata M, Abe Y, Hino T, Ikeda-Suno C, and Kuma H (2015). Crystal structure of the anion exchanger domain of human erythrocyte band 3. Science 350, 680–684. [PubMed: 26542571]

Asarnow D, Palovcak E, Cheng Y (2019). UCSF pyem v0.5. Zenodo https://doiorg/105281/zenodo3576630.

Ashmore J (1987). A fast motile response in guinea-pig outer hair cells: the cellular basis of the cochlear amplifier. The Journal of Physiology 388, 323–347. [PubMed: 3656195]

Ashmore J (2019). Outer hair cells and electromotility. Cold Spring Harbor perspectives in medicine 9, a033522. [PubMed: 30181355]

Bai JP, Navaratnam D, Samaranayake H, and Santos-Sacchi J (2006). En block C-terminal charge cluster reversals in prestin (SLC26A5): effects on voltage-dependent electromechanical activity. Neurosci Lett 404, 270–275. [PubMed: 16839688]

Bai JP, Surguchev A, Montoya S, Aronson PS, Santos-Sacchi J, and Navaratnam D (2009). Prestin's anion transport and voltage-sensing capabilities are independent. Biophys J 96, 3179–3186. [PubMed: 19383462]

Bennett CH (1976). Efficient estimation of free energy differences from Monte Carlo data. Journal of Computational Physics 22, 245–268.

Brownell WE, Bader CR, Bertrand D, and De Ribaupierre Y (1985). Evoked mechanical responses of isolated cochlear outer hair cells. Science 227, 194–196. [PubMed: 3966153]

Cannon WR, Pettitt BM, and McCammon JA (1994). Sulfate anion in water: model structural, thermodynamic, and dynamic properties. The Journal of Physical Chemistry 98, 6225–6230.

Chen H, Maia JD, Radak BK, Hardy DJ, Cai W, Chipot C, and Tajkhorshid E (2020). Boosting Free-Energy Perturbation Calculations with GPU-Accelerated NAMD. Journal of Chemical Information and Modeling 60, 5301–5307. [PubMed: 32805108]

Chi X, Jin X, Chen Y, Lu X, Tu X, Li X, Zhang Y, Lei J, Huang J, Huang Z, et al. (2020). Structural insights into the gating mechanism of human SLC26A9 mediated by its C-terminal sequence. Cell Discov 6, 55. [PubMed: 32818062]

Cournia Z, Allen B, and Sherman W (2017). Relative binding free energy calculations in drug discovery: recent advances and practical considerations. Journal of chemical information and modeling 57, 2911–2937. [PubMed: 29243483]

Dallos P (2008). Cochlear amplification, outer hair cells and prestin. Current opinion in neurobiology 18, 370–376. [PubMed: 18809494]

Dallos P, and Fakler B (2002). Prestin, a new type of motor protein. Nature Reviews Molecular Cell Biology 3, 104–111. [PubMed: 11836512]

Dallos P, Zheng J, and Cheatham MA (2006). Prestin and the cochlear amplifier. J Physiol 576, 37–42. [PubMed: 16873410]

Darden T, York D, and Pedersen L (1993). Particle mesh Ewald: An N· log (N) method for Ewald sums in large systems. The Journal of chemical physics 98, 10089–10092.

Emsley P, and Cowtan K (2004). Coot: model-building tools for molecular graphics. Acta Crystallogr D Biol Crystallogr 60, 2126–2132. [PubMed: 15572765]

Emsley P, Lohkamp B, Scott WG, and Cowtan K (2010). Features and development of Coot. Acta Crystallographica Section D: Biological Crystallography 66, 486–501. [PubMed: 20383002]

Fang J, Izumi C, and Iwasa KH (2010). Sensitivity of prestin-based membrane motor to membrane thickness. Biophys J 98, 2831–2838. [PubMed: 20550895]

Feller SE, Zhang Y, Pastor RW, and Brooks BR (1995). Constant pressure molecular dynamics simulation: the Langevin piston method. The Journal of chemical physics 103, 4613–4621.

Fiorin G, Klein ML, and Hénin J (2013). Using collective variables to drive molecular dynamics simulations. Molecular Physics 111, 3345–3362.

Forge A (1991). Structural features of the lateral walls in mammalian cochlear outer hair cells. Cell and tissue research 265, 473–483. [PubMed: 1786594]

Gale JE, and Ashmore JF (1997). The outer hair cell motor in membrane patches. Pflugers Arch 434, 267–271. [PubMed: 9178625]

Ge J, Li W, Zhao Q, Li N, Chen M, Zhi P, Li R, Gao N, Xiao B, and Yang M (2015). Architecture of the mammalian mechanosensitive Piezo1 channel. Nature 527, 64–69. [PubMed: 26390154]

Gillis KD (2000). Admittance-based measurement of membrane capacitance using the EPC-9 patch-clamp amplifier. Pflügers Archiv 439, 655–664. [PubMed: 10764227]

Goddard TD, Huang CC, Meng EC, Pettersen EF, Couch GS, Morris JH, and Ferrin TE (2018). UCSF ChimeraX: Meeting modern challenges in visualization and analysis. Protein Sci 27, 14–25. [PubMed: 28710774]

Goehring A, Lee CH, Wang KH, Michel JC, Claxton DP, Baconguis I, Althoff T, Fischer S, Garcia KC, and Gouaux E (2014). Screening and large-scale expression of membrane proteins in mammalian cells for structural studies. Nat Protoc 9, 2574–2585. [PubMed: 25299155]

Gorbunov D, Sturlese M, Nies F, Kluge M, Bellanda M, Battistutta R, and Oliver D (2014). Molecular architecture and the structural basis for anion interaction in prestin and SLC26 transporters. Nat Commun 5, 3622. [PubMed: 24710176]

Gumbart J, Trabuco LG, Schreiner E, Villa E, and Schulten K (2009). Regulation of the protein-conducting channel by a bound ribosome. Structure 17, 1453–1464. [PubMed: 19913480]

Gummer AW, and Preyer S (1997). Cochlear amplification and its pathology: emphasis on the role of the tectorial membrane. Ear Nose Throat J 76, 151–158, 160, 162–153. [PubMed: 9086644]

Guo P, Noji H, Yengo CM, Zhao Z, and Grainge I (2016). Biological Nanomotors with a Revolution, Linear, or Rotation Motion Mechanism. Microbiology and Molecular Biology Reviews 80, 161–186. [PubMed: 26819321]

Guo YR, and MacKinnon R (2017). Structure-based membrane dome mechanism for Piezo mechanosensitivity. Elife 6.

Hallworth R, and Nichols MG (2012). Prestin in HEK cells is an obligate tetramer. J Neurophysiol 107, 5–11. [PubMed: 21975444]

Homma K, and Dallos P (2011). Evidence that prestin has at least two voltage-dependent steps. Journal of Biological Chemistry 286, 2297–2307.

Homma K, Duan C, Zheng J, Cheatham MA, and Dallos P (2013). The V499G/Y501H mutation impairs fast motor kinetics of prestin and has significance for defining functional independence of individual prestin subunits. J Biol Chem 288, 2452–2463. [PubMed: 23212912]

Huang G, and Santos-Sacchi J (1993). Mapping the distribution of the outer hair cell motility voltage sensor by electrical amputation. Biophys J 65, 2228–2236. [PubMed: 8298046]

Huang J, Rauscher S, Nawrocki G, Ran T, Feig M, de Groot BL, Grubmuller H, and MacKerell AD Jr. (2017). CHARMM36m: an improved force field for folded and intrinsically disordered proteins. Nat Methods 14, 71–73. [PubMed: 27819658]

Humphrey W, Dalke A, and Schulten K (1996). VMD: visual molecular dynamics. J Mol Graph 14, 33–38, 27–38.

Iwasa KH (1993). Effect of stress on the membrane capacitance of the auditory outer hair cell. Biophys J 65, 492–498. [PubMed: 8369452]

Iwasa KH (1994). A membrane motor model for the fast motility of the outer hair cell. J Acoust Soc Am 96, 2216–2224. [PubMed: 7963034]

Jo S, Kim T, Iyer VG, and Im W (2008). CHARMM-GUI: a web-based graphical user interface for CHARMM. J Comput Chem 29, 1859–1865. [PubMed: 18351591]

Jorgensen WL, Chandrasekhar J, Madura JD, Impey RW, and Klein ML (1983). Comparison of simple potential functions for simulating liquid water. The Journal of chemical physics 79, 926–935.

Kakehata S, and Santos-Sacchi J (1996). Effects of salicylate and lanthanides on outer hair cell motility and associated gating charge. Journal of Neuroscience 16, 4881–4889. [PubMed: 8756420]

Kamar R, Organ-Darling L, and Raphael R (2012). Membrane cholesterol strongly influences confined diffusion of prestin. Biophysical Journal 103, 1627–1636. [PubMed: 23083705]

Klauda JB, Venable RM, Freites JA, O'Connor JW, Tobias DJ, Mondragon-Ramirez C, Vorobyov I, MacKerell AD Jr., and Pastor RW (2010). Update of the CHARMM all-atom additive force field for lipids: validation on six lipid types. J Phys Chem B 114, 7830–7843. [PubMed: 20496934]

Liberman MC, Gao J, He DZ, Wu X, Jia S, and Zuo J (2002). Prestin is required for electromotility of the outer hair cell and for the cochlear amplifier. Nature 419, 300–304. [PubMed: 12239568]

Liebschner D, Afonine PV, Baker ML, Bunkóczi G, Chen VB, Croll TI, Hintze B, Hung L-W, Jain S, and McCoy AJ (2019). Macromolecular structure determination using X-rays, neutrons and electrons: recent developments in Phenix. Acta Crystallographica Section D: Structural Biology 75, 861–877. [PubMed: 31588918]

Liu P, Dehez F.o., Cai W, and Chipot C (2012). A toolkit for the analysis of free-energy perturbation calculations. Journal of chemical theory and computation 8, 2606–2616. [PubMed: 26592106]

Lolli G, Pasqualetto E, Costanzi E, Bonetto G, and Battistutta R (2016). The STAS domain of mammalian SLC26A5 prestin harbours an anion-binding site. Biochemical Journal 473, 365–370.

Lomize MA, Lomize AL, Pogozheva ID, and Mosberg HI (2006). OPM: orientations of proteins in membranes database. Bioinformatics 22, 623–625. [PubMed: 16397007]

Lu F, Li S, Jiang Y, Jiang J, Fan H, Lu G, Deng D, Dang S, Zhang X, Wang J, et al. (2011). Structure and mechanism of the uracil transporter UraA. Nature 472, 243–246. [PubMed: 21423164]

Mahendrasingam S, Beurg M, Fettiplace R, and Hackney CM (2010). The ultrastructural distribution of prestin in outer hair cells: a post-embedding immunogold investigation of low-frequency and high-frequency regions of the rat cochlea. European journal of neuroscience 31, 1595–1605.

Martyna GJ, Tobias DJ, and Klein ML (1994). Constant pressure molecular dynamics algorithms. The Journal of chemical physics 101, 4177–4189.

Mastronarde DN (2005). Automated electron microscope tomography using robust prediction of specimen movements. Journal of structural biology 152, 36–51. [PubMed: 16182563]

Mayne CG, Saam J, Schulten K, Tajkhorshid E, and Gumbart JC (2013). Rapid parameterization of small molecules using the force field toolkit. Journal of computational chemistry 34, 2757–2770. [PubMed: 24000174]

Mongan E, Kelly P, Nies K, Porter WW, and Paulus HE (1973). Tinnitus as an indication of therapeutic serum salicylate levels. Jama 226, 142–145. [PubMed: 4740906]

Muallem D, and Ashmore J (2006). An anion antiporter model of prestin, the outer hair cell motor protein. Biophysical journal 90, 4035–4045. [PubMed: 16565043]

Mutai H, Suzuki N, Shimizu A, Torii C, Namba K, Morimoto N, Kudoh J, Kaga K, Kosaki K, and Matsunaga T (2013). Diverse spectrum of rare deafness genes underlies early-childhood hearing loss in Japanese patients: a cross-sectional, multi-center next-generation sequencing study. Orphanet journal of rare diseases 8, 172. [PubMed: 24164807]

MYERS EN, and BERNSTEIN JM (1965). Salicylate ototoxicity: a clinical and experimental study. Archives of Otolaryngology 82, 483–493. [PubMed: 4954319]

Navaratnam D, Bai J-P, Samaranayake H, and Santos-Sacchi J (2005). N-terminal-mediated homomultimerization of prestin, the outer hair cell motor protein. Biophysical journal 89, 3345–3352. [PubMed: 16113116]

Oliver D, He DZ, Klöcker N, Ludwig J, Schulte U, Waldegger S, Ruppersberg J, Dallos P, and Fakler B (2001). Intracellular anions as the voltage sensor of prestin, the outer hair cell motor protein. Science 292, 2340–2343. [PubMed: 11423665]

Olsson MH, Sondergaard CR, Rostkowski M, and Jensen JH (2011). PROPKA3: Consistent Treatment of Internal and Surface Residues in Empirical pKa Predictions. J Chem Theory Comput 7, 525–537. [PubMed: 26596171]

Pettersen EF, Goddard TD, Huang CC, Couch GS, Greenblatt DM, Meng EC, and Ferrin TE (2004). UCSF Chimera--a visualization system for exploratory research and analysis. J Comput Chem 25, 1605–1612. [PubMed: 15264254]

Pettersen EF, Goddard TD, Huang CC, Meng EC, Couch GS, Croll TI, Morris JH, and Ferrin TE (2020). UCSF ChimeraX: Structure visualization for researchers, educators, and developers. Protein Science.

Phillips JC, Braun R, Wang W, Gumbart J, Tajkhorshid E, Villa E, Chipot C, Skeel RD, Kale L, and Schulten K (2005). Scalable molecular dynamics with NAMD. J Comput Chem 26, 1781–1802. [PubMed: 16222654]

Phillips JC, Hardy DJ, Maia JDC, Stone JE, Ribeiro JV, Bernardi RC, Buch R, Fiorin G, Henin J, Jiang W, et al. (2020). Scalable molecular dynamics on CPU and GPU architectures with NAMD. J Chem Phys 153, 044130. [PubMed: 32752662]

Punjani A, Rubinstein JL, Fleet DJ, and Brubaker MA (2017). cryoSPARC: algorithms for rapid unsupervised cryo-EM structure determination. Nature methods 14, 290–296. [PubMed: 28165473]

Punjani A, Zhang H, and Fleet DJ (2019). Non-uniform refinement: Adaptive regularization improves single particle cryo-EM reconstruction. BioRXiv.

Rajagopalan L, Greeson JN, Xia A, Liu H, Sturm A, Raphael RM, Davidson AL, Oghalai JS, Pereira FA, and Brownell WE (2007). Tuning of the outer hair cell motor by membrane cholesterol. Journal of Biological Chemistry 282, 36659–36670.

Rubinstein JL, and Brubaker MA (2015). Alignment of cryo-EM movies of individual particles by optimization of image translations. Journal of structural biology 192, 188–195. [PubMed: 26296328]

Rybalchenko V, and Santos-Sacchi J (2003). Allosteric modulation of the outer hair cell motor protein prestin by chloride. In Biophysics of the Cochlea: From Molecules to Models (World Scientific), pp. 116–126.

Rybalchenko V, and Santos-Sacchi J (2008a). Anion control of voltage sensing by the motor protein prestin in outer hair cells. Biophys J 95, 4439–4447. [PubMed: 18658219]

Rybalchenko V, and Santos-Sacchi J (2008b). Anion control of voltage sensing by the motor protein prestin in outer hair cells. Biophysical journal 95, 4439–4447. [PubMed: 18658219]

Ryckaert J-P, Ciccotti G, and Berendsen HJ (1977). Numerical integration of the cartesian equations of motion of a system with constraints: molecular dynamics of n-alkanes. Journal of computational physics 23, 327–341.

Santos-Sacchi J (1991). Reversible inhibition of voltage-dependent outer hair cell motility and capacitance. Journal of Neuroscience 11, 3096–3110. [PubMed: 1941076]

Santos-Sacchi J, Kakehata S, Kikuchi T, Katori Y, and Takasaka T (1998). Density of motility-related charge in the outer hair cell of the guinea pig is inversely related to best frequency. Neuroscience letters 256, 155–158. [PubMed: 9855363]

Santos-Sacchi J, Navaratnam D, Raphael R, and Oliver D (2017). Prestin: molecular mechanisms underlying outer hair cell electromotility. In Understanding the Cochlea (Springer), pp. 113–145.

Santos-Sacchi J, Shen W, Zheng J, and Dallos P (2001). Effects of membrane potential and tension on prestin, the outer hair cell lateral membrane motor protein. J Physiol 531, 661–666. [PubMed: 11251048]

Santos-Sacchi J, and Song L (2014). Chloride and salicylate influence prestin-dependent specific membrane capacitance: support for the area motor model. J Biol Chem 289, 10823–10830. [PubMed: 24554714]

Santos-Sacchi J, and Song L (2016). Chloride anions regulate kinetics but not voltage-sensor Qmax of the solute carrier SLC26a5. Biophysical journal 110, 2551–2561. [PubMed: 27276272]

Santos-Sacchi J, Song L, Zheng J, and Nuttall AL (2006). Control of mammalian cochlear amplification by chloride anions. Journal of Neuroscience 26, 3992–3998. [PubMed: 16611815]

Santos-Sacchi J, and Tan W (2020). Complex nonlinear capacitance in outer hair cell macro-patches: effects of membrane tension. Sci Rep 10, 6222. [PubMed: 32277153]

Saotome K, Murthy SE, Kefauver JM, Whitwam T, Patapoutian A, and Ward AB (2018). Structure of the mechanically activated ion channel Piezo1. Nature 554, 481–486. [PubMed: 29261642]

Schaechinger TJ, Gorbunov D, Halaszovich CR, Moser T, Kugler S, Fakler B, and Oliver D (2011). A synthetic prestin reveals protein domains and molecular operation of outer hair cell piezoelectricity. EMBO J 30, 2793–2804. [PubMed: 21701557]

Sfondouris J, Rajagopalan L, Pereira FA, and Brownell WE (2008). Membrane composition modulates prestin-associated charge movement. Journal of Biological Chemistry 283, 22473–22481.

Sondergaard CR, Olsson MH, Rostkowski M, and Jensen JH (2011). Improved Treatment of Ligands and Coupling Effects in Empirical Calculation and Rationalization of pKa Values. J Chem Theory Comput 7, 2284–2295. [PubMed: 26606496]

Song L, and Santos-Sacchi J (2010). Conformational state-dependent anion binding in prestin: evidence for allosteric modulation. Biophysical journal 98, 371–376. [PubMed: 20141749]

Song L, and Santos-Sacchi J (2013). Disparities in voltage-sensor charge and electromotility imply slow chloride-driven state transitions in the solute carrier SLC26a5. Proceedings of the National Academy of Sciences 110, 3883–3888.

Swartz KJ (2008). Sensing voltage across lipid membranes. Nature 456, 891–897. [PubMed: 19092925]

Takahashi S, Cheatham MA, Zheng J, and Homma K (2016). The R130S mutation significantly affects the function of prestin, the outer hair cell motor protein. J Mol Med (Berl) 94, 1053–1062. [PubMed: 27041369]

Tan X, Pecka JL, Tang J, Lovas S, Beisel KW, and He DZ (2012). A motif of eleven amino acids is a structural adaptation that facilitates motor capability of eutherian prestin. Journal of cell science 125, 1039–1047. [PubMed: 22399806]

Vanommeslaeghe K, Hatcher E, Acharya C, Kundu S, Zhong S, Shim J, Darian E, Guvench O, Lopes P, Vorobyov I, et al. (2010). CHARMM general force field: A force field for drug-like molecules compatible with the CHARMM all-atom additive biological force fields. J Comput Chem 31, 671–690. [PubMed: 19575467]

Vanommeslaeghe K, Raman EP, and MacKerell AD Jr. (2012). Automation of the CHARMM General Force Field (CGenFF) II: assignment of bonded parameters and partial atomic charges. J Chem Inf Model 52, 3155–3168. [PubMed: 23145473]

Walter JD, Sawicka M, and Dutzler R (2019). Cryo-EM structures and functional characterization of murine Slc26a9 reveal mechanism of uncoupled chloride transport. Elife 8.

Zhang L, and Hermans J (1996). Hydrophilicity of cavities in proteins. Proteins 24, 433–438. [PubMed: 9162944]

Zhao Z, and Tajkhorshid E (2021). GOLEM: Automated and Robust Cryo-EM-Guided Ligand Docking with Explicit Water Molecules. Biophysical Journal 120, 290a.

Zheng J, Du GG, Anderson CT, Keller JP, Orem A, Dallos P, and Cheatham M (2006). Analysis of the oligomeric structure of the motor protein prestin. J Biol Chem 281, 19916–19924. [PubMed: 16682411]

Zheng J, Shen W, He DZ, Long KB, Madison LD, and Dallos P (2000). Prestin is the motor protein of cochlear outer hair cells. Nature 405, 149–155. [PubMed: 10821263]

Zivanov J, Nakane T, Forsberg BO, Kimanius D, Hagen WJ, Lindahl E, and Scheres SH (2018). New tools for automated high-resolution cryo-EM structure determination in RELION-3. Elife 7.

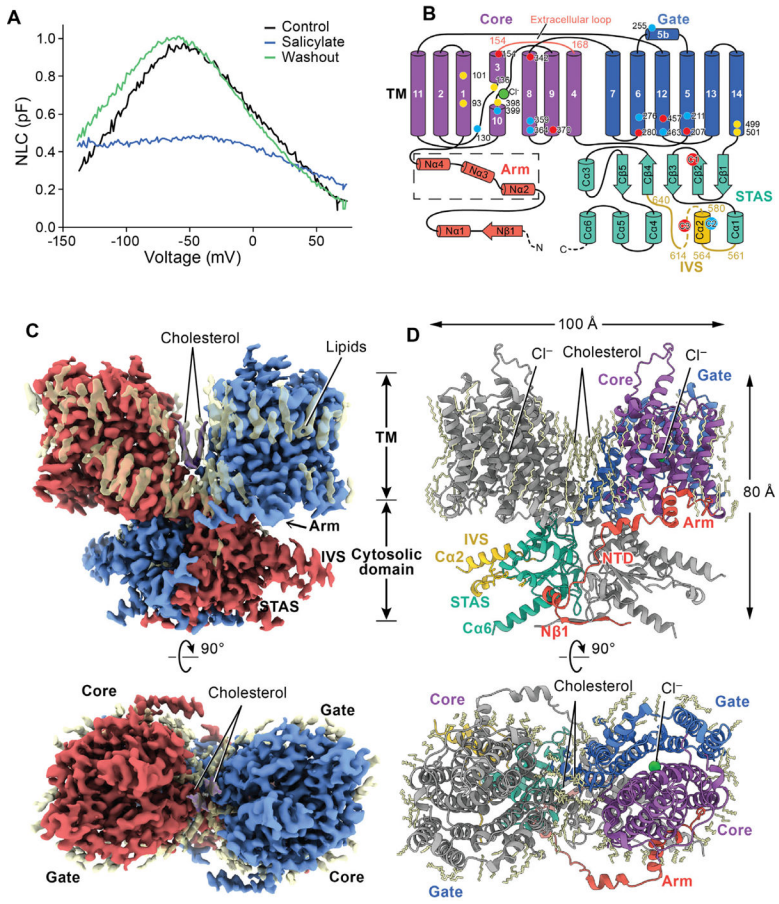

Figure 1. Function and cryo-EM structure of human prestin.

A. Non-linear capacitance measurement of HEK293 cells expressing human prestin.

B. Schematic of the prestin secondary structure features. The features are colored based on panel D. Chloride is shown as a green dot. Neutral, positively and negatively charged residues that affect the prestin NLC in previous studies are shown as yellow, blue and red dots, respectively.

C. Cryo-EM maps of prestin bound with chloride (Pres-Cl). The two protomers are colored red and blue. Resolved lipid molecules are shown in a transparent yellow surface. Densities representing cholesterol molecules are colored in purple.

D. Structural model of Pres-Cl shown in ribbon representation. Key domains are colored in a single protomer.

See also Figures S1–S7

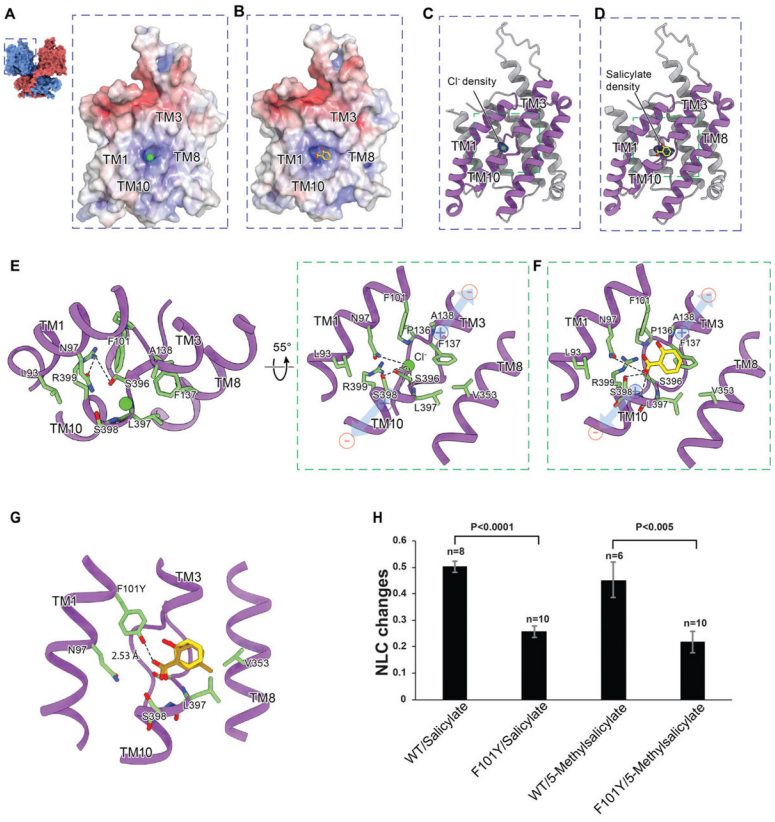

Figure 2. Anion binding pocket.

A-B. Electrostatic potential surfaces of the core domain of the Pres-Cl (A) and Pres-Sal (B) structures. Cl^- is shown as a green sphere. Salicylate is shown as sticks.

C-D. Cartoon representation of the anion binding pocket of the Pres-Cl (**C**) and the Pres-Sal (**D**) structures. The core domain from one TMD is shown in each panel. Helices flanking the anion binding site are colored in purple. The cryo-EM densities of Cl^- or salicylate anion are shown as mesh.

E. Details of the Cl^- binding pocket of Pres-Cl. Left panel, interactions of R399 proximal to the pocket. Right panel, interactions between the Cl^- ion and surrounding hydrophilic residues. Blue arrows indicate the helical dipoles of TMs 3 and 10.

F. Details of the salicylate binding pocket of Pres-Sal.

G. Computational model of the prestin F101Y mutant and binding of 5-methylsalicylate.

H. Measurements of changes in NLC amplitude upon application of 10mM of either salicylate or 5-methylsalicylate in cells transfected with WT prestin or the F101Y mutant.

See also Figures S1, S2, S4, S8, S9

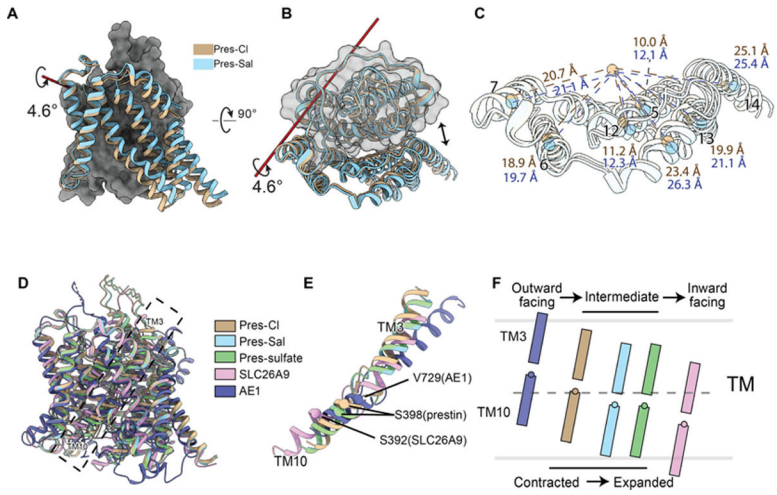

Figure 3. Chloride and salicylate stabilize distinct TMD conformations.

A-C. Conformational differences in the TMDs of the Pres-Cl and Pres-Sal complexes. TMDs from one protomer of Pres-Cl and Pres-Sal were superimposed based on the core domain. (**A**) The gate domain, shown as cartoon, has a 4.6° rotation around an axis approximately parallel to the membrane (labeled in red). The core domains are shown as grey surfaces. (**B**) A 90° rotated view of (**A**) showing the separation of the core and gate domains in Pres-Sal relative to Pres-Cl. (**C**) Distance measurements between the anion binding site, defined by the center of mass of residues 396–398, and the center of mass of each helix in the gate domain of Pres-Cl and Pres-Sal.

D-F. Structural comparisons of prestin structures with homologous proteins. (**D**) Structural comparison of Pres-Cl, Pres-Sal, Pres-sulfate, the inward-facing state of SLC26A9 (PDB:7CH1) and the outward-facing state of AE1 (PDB: 4YZF). The structures are superimposed based on the gate domain. (**E**) View of TMs 3 and 10 that form the anion binding pocket. A key anion binding residue S398 in prestin and its equivalent residues V729 in AE1 and S392 in SLC26A9 are labeled. (**F**) Schematic representation showing how the different prestin conformational states correspond to conformations of homologous transporter proteins.

See also Figures S8, S10, S11

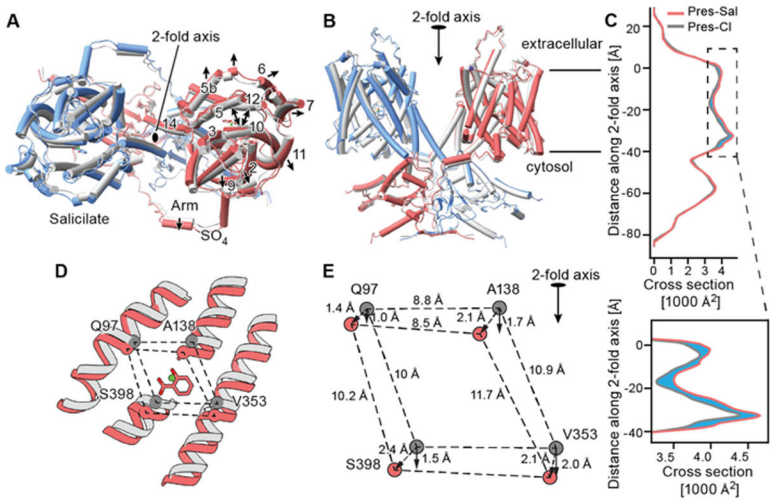

Figure 4. Prestin adopts an expanded conformation in the absence of chloride.

A-B. Tube representation of Pres-Sal (colored blue and red for each chain) or Pres-Cl (grey), superimposed based on the STAS domain.

C. Cross sectional area of the prestin dimer in Pres-Sal and Pres-Cl, measured along the two-fold axis using a thresholded Gaussian map (Supplemental Information).

D. Conformational displacements of the anion binding site relative to the STAS domain between Pres-Sal (colored) and Pres-Cl (grey). Cα atoms of residues used to measure displacements are indicated by spheres. **E.** Schematic representation of the displacement of the four residues highlighted in panel D. Dashed lines indicate distances between the Cα atoms within each state. Dashed arrows indicate the absolute distance between Cα atoms of each residue between Pres-Sal and Pres-Cl. Solid arrows indicate the component of the same distance along the two-fold axis.

See also Figures S11, 12, Movie S1

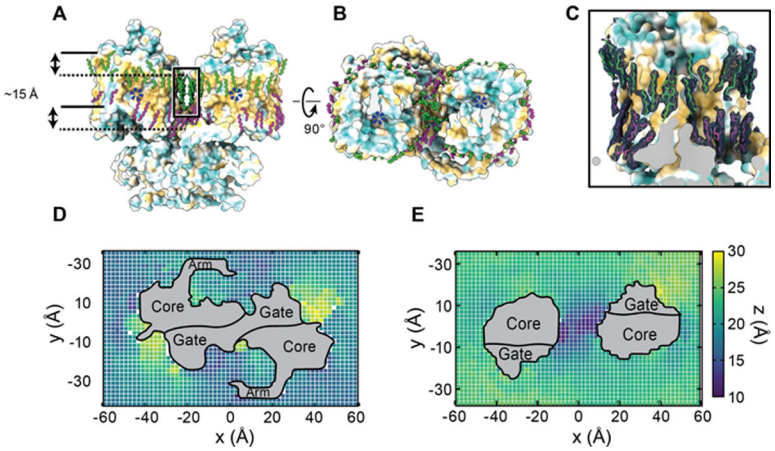

Figure 5. Prestin deforms the lipid bilayer.

A-B. Pres-Cl, solved in the presence of GDN, shown in surface representation where the surface is colored based on lipophilicity, from gold (lipophilic) to blue (hydrophilic). Modeled lipids from the upper leaflet are shown as green sticks and lipids from the lower leaflet are shown as magenta sticks. The position of the chloride atom is indicated using a blue mark.

C. View of the TMD of a single prestin protomer together with modeled lipids and their corresponding cryo-EM density (blue mesh). The density modeled as cholesterol is substantially flatter than other lipid densities.

D-E. Heatmaps of the average lipid headgroup height during a 1.5-μs MD simulation in the lower leaflet (**D**) and upper leaflet (**E**).

See also Figures S3, S4

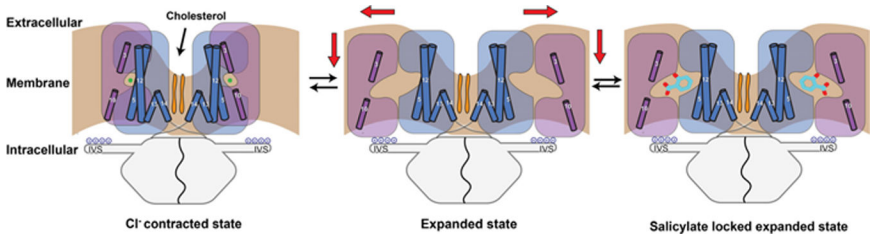

Figure 6. Mechanism of prestin.

Left, prestin is in a contracted state in the presence of Cl^-. A saddle-shaped membrane is formed around prestin. Two cholesterol molecules are bound in the center gap between the TMDs and the lower point of the upper membrane. Middle, absence of Cl^- induces both the expansion of the TMDs and the elevation of the core domain including the anion-binding pocket. Right, salicylate locks prestin in the expanded state. The binding of salicylate does not permit contraction, thus inhibiting the eM function of prestin.

KEY RESOURCES TABLE

REAGENT or RESOURCE	SOURCE	IDENTIFIER
Chemicals and Recombinant Proteins		
Sf-900™ III SFM (1X)	GIBCO	Cat#12658-027
FreeStyle-293 Expression Medium	GIBCO	Cat#12338-026
Sodium salicylate	Sigma	Cat#S3007
Lipofectamine 2000 reagent	Invitrogen	Cat#11668-027
Cellfectin II reagent	Invitrogen	Cat#10362-100
Digitonin	Millipore	Cat#300410
GDN	Anatrace	CAT#GDN101 5gm
CHS	Anatrace	Cat#CH210 25GM
Deposited Data		
Pres-Cl, chloride, contracted state, micelle	This Study	PDB ID: 7LGU, EMDB ID: EMD-23329
Pres-Cl-nanodisc, chloride, contracted state, nanodisc	This Study	PDB ID: 7LGW, EMDB ID: EMD-23331
Pres-Sal, salicylate, expanded state, micell	This Study	PDB ID: 7LH2, EMDB ID: EMD-23334
Pres-sulfate, sulfate, expanded state, micell	This Study	PDB ID: 7LH3, EMDB ID: EMD-23335
Recombinant DNA		
pEG_BacMam-CMV-hPrestin-GFP-strep	This Study	N/A
Experimental Models: Cell lines		
HEK293S GnTI^{-}	ATCC	CRL-3022
Sf9	ATCC	CRL-1711
Software and Algorithms		
SerialEM	(Mastronarde, 2005)	https://bio3d.colorado.edu/SerialEM/
RELION 3.1	(Zivanov et al., 2018)	https://www3.mrc-lmb.cam.ac.uk/relion/index.php/Main_Page
CryoSparc	(Punjani et al., 2017)	https://cryosparc.com
Phenix	(Afonine et al., 2018)	https://www.phenix-online.org
UCSF Chimera	(Pettersen et al., 2004)	https://www.cgl.ucsf.edu/chimera
UCSF ChimeraX	(Goddard et al., 2018)	https://www.rbvi.ucsf.edu/chimerax
COOT	(Emsley and Cowtan, 2004)	https://www2.mrc-lmb.cam.ac.uk/personal/pemsley/coot
PyMOL	Schrodinger	https://pymol.org/2
PSFGEN	(Humphrey et al., 1996)	https://www.ks.uiuc.edu/Research/vmd/plugins/psfgen/
VMD	(Humphrey et al., 1996)	http://www.ks.uiuc.edu/Research/vmd/
PROPKA 3.1	(Olsson et al., 2011; Sondergaard et al., 2011)	https://github.com/jensengroup/propka-3.1
Dowser	(Gumbart et al., 2009; Zhang and Hermans, 1996)	https://www.ks.uiuc.edu/Research/vmd/plugins/dowser/

REAGENT or RESOURCE	SOURCE	IDENTIFIER
CHARMM-GUI	(Jo et al., 2008)	http://www.charmm-gui.org
OPM	(Lomize et al., 2006)	https://opm.phar.umich.edu
GOLEM	(Zhao and Tajkhorshid, 2021)	www.ks.uiuc.edu/Research/GOLEM
NAMD	(Phillips et al., 2005)	http://www.ks.uiuc.edu/Research/namd/
CGenFF	(Vanommeslaeghe et al., 2010; Vanommeslaeghe et al., 2012)	https://cgenff.paramchem.org
Force Field Toolkit (ffTK)	(Mayne et al., 2013)	http://www.ks.uiuc.edu/Research/vmd/plugins/fftk/
Other		
Strep-Tactin® Superflow® high capacity resin	IBA	Cat# 2-1208-002
R2/2 200 mesh Au holey carbon grids	TedPella	Cat#657-200-AU-100